*Journal of The Electrochemical Society*, **166** (15) A1-A12 (2019)
0013-4651/2019/166(15)/A1/12/$38.00 © The Electrochemical Society



# Advancing Lithium- and Manganese-Rich Cathodes through a Combined Electrolyte Additive/Surface Treatment Strategy

**Arturo Gutierrez,[1] Meinan He,[1] Bryan T. Yonemoto,[2] Zhenzhen Yang,[1] Jie Wang,[3] Harry M. Meyer III,[4] Michael M. Thackeray,[1,*] and Jason R. Croy[1,z]**

[1]*Electrochemical Energy Storage Department, Chemical Sciences and Engineering Division, Argonne National Laboratory, Lemont, Illinois 60439, USA*
[2]*Microvast Power Solutions, Inc., Orlando, Florida 32826, USA*
[3]*Thorlabs Quantum Electronics Inc., Jessup, Maryland 20794, USA*
[4]*Materials Science and Technology Division, Oak Ridge National Laboratory, Oak Ridge, Tennessee 37831, USA*

Lithium- and manganese-rich (LMR) materials provide cost and environmental advantages to other competing cathodes based on nickel or cobalt chemistries. Within the LMR family, layered-layered-spinel (LLS) cathodes have unique properties, detailed herein, that address several of the challenges faced in large-scale implementation of LMR cathodes. This paper details how a LLS//graphite system was considerably improved by combining optimization strategies. First, a cathode surface-treatment process was optimized. Interestingly, cathodes surface-treated at a low temperature (~100°C) exhibited the best results. The optimized LLS cathode was tested vs. graphite using small amounts of lithium difluoro(oxalate)borate electrolyte additive. The combined approach improved various aspects of the electrochemical performance (e.g., impedance, cycle life, and coulombic efficiency) more than each strategy used alone by mitigating Mn dissolution from the cathode and the ensuing re-deposition on the anode. The report describes a unique method to improve the performance of practically relevant LMR//graphite cells.
 [DOI: 10.1149/2.1281915jes]

Manuscript submitted September 9, 2019; revised manuscript received October 9, 2019. Published 00 0, 2019.

It is hard to imagine the world without lithium-ion batteries (LIBs). In fact, there is a generation of young adults now *un*familiar with life before there were portable electronics powered by LIBs. They are ubiquitous in our lives. Electrification of the transportation sector is clearly the next frontier for LIBs in the form of mass implementation of electric vehicles (EVs). However, deep market penetration of EVs is dependent on improved technology, especially with respect to the cost of the cathode materials. One of the most promising classes of cathode materials being pursued for "next-generation" LIBs is the Li- and Mn-rich, "layered-layered" class of composite oxides (denoted as LMR from here forward). These oxides have the general formula, $xLi_2MnO_3$•(1-x)$NMCO_2$ (where NMC=Ni, Mn, Co), and can achieve reversible capacities of 250–300 mAh/g,[1,2] substantially higher than competing cathodes (i.e., $LiCoO_2$, $LiMn_2O_4$, $LiNi_{1/3}Mn_{1/3}Co_{1/3}O_2$ and $LiFePO_4$), which deliver capacities $\leq$ 180 mAh $g^{-1}$. With an average working potential of ~3.7 V (vs. $Li^+/Li^0$), LMR oxides are able to deliver notable energy densities of 900–1000 Wh/$kg_{oxide}$ at beginning of life. Furthermore, the inherent safety properties and low cost of LMR materials make them a leading candidate as cathodes in EV batteries.

Yet, some challenges still hinder penetration of high-capacity (e.g., x > ~0.1) LMR cathodes in the EV market. First, the higher capacities associated with the composite material are related to the oxidation of oxygen ions in the lattice during the initial charge above 4.5 V vs. $Li^+/Li^0$.[3] This process induces oxygen evolution and transition-metal migration, both of which lead to structural instability at the electrode surface within the bulk. The composite material undergoes further degradation upon subsequent cycling, including a decrease in the average voltage and voltage hysteresis that ultimately lowers the output energy of the system.[4] These structural deficiencies, accompanied by poor electrical conductivity and a low first cycle efficiency (FCE), have left the research community in search of an approach to slow the structural degradation. One approach has been to integrate a spinel component into the LMR parent material to form a complex layered-layered-spinel (LLS) composite structure y[$xLi_2MnO_3$•(1-x)$NMCO_2$]•(1-y)$Li(NMC)_2O_4$.[5–7] It has been demonstrated that by controlling the percent of spinel component, one can improve the FCE (to >90%), cycle life, and rate capability.[6] The improvement to the electrochemical performance brought about by the addition of a spinel component is attributed to: i.) unoccupied octahedral sites in the spinel structure, which help to offset the poor FCE characteristic of the LMR materials, ii.) a barrier to transition metal (TM) migration associated with the alternating ratio of 3:1 between Li:TM, and iii.) a three-dimensional pathway for lithium diffusion, which may lead to improved rate capability.

In addition to bulk instabilities of the LMR composite electrode structure, evidenced by voltage fade and hysteresis, a structural rearrangement of the *surface* occurs when the electrode is cycled to high voltages. The evolution of oxygen during the first charge above 4.5 V initiates a surface reconstruction involving cation migration between the Li/TM layers.[8] Along with the evolution of $O_2$ gas, it has been proposed that oxygen radicals are formed, leading to the decomposition of the carbonate-based electrolyte and the formation of byproducts, including $Li_2CO_3$[9,10] and HF,[11] which are detrimental to the performance of the cathode. Due to these surface volatilities, countless surface treatments/coatings have been used to mitigate the negative effects of an unstable surface. The treatments have included carbon,[12,13] phosphate,[14,15] oxide,[16,17] fluoride,[18] polymer,[19] and even electrolyte additives.[20] Each treatment has distinct properties thought to improve the performance of the cathode material. In general, most surface treatments for LMR cathodes found in the literature are carried out vs. Li metal anodes, whereas current state-of-the-art LIBs use graphite as the anode material. Graphite anodes have been linked to unwanted side reactions that result in the trapping of lithium ions, one of the main causes of capacity fade in practical cells.[21] Such effects are poorly accounted for in lithium-metal cells with large reserves of available lithium. Therefore, although some reported treatments may provide some level of performance improvement of the cathode itself, their effectiveness to improve overall cell performance under practical conditions remains unsubstantiated.

In this paper, we report on one of the several surface-stabilization strategies being pursued by our team at Argonne National Laboratory to improve the performance of LMR//graphite cells under more practical conditions.[22] A baseline LLS cathode material, with composition $0.94[0.25Li_2MnO_3•0.75LiMn_{0.375}Ni_{0.375}Co_{0.25}O_2]•0.06Li(NMC)_2O_4$ as described by Long et al.,[7] was chosen for this study. The approach taken here combines the optimization of the electrolyte through the use of lithium difluoro(oxalate)borate (LiDFOB) as an additive combined with a low-temperature cathode surface treatment based on metal precursors (e.g., nitrates) in solution. The use of metals such as Al, Mg, and Ti in surface treatments has been investigated on a wide range of cathode chemistries, including $LiCoO_2$,[23] $LiMn_{1.5}Ni_{0.5}O_4$,[24,25] and LMR (layered-layered) systems.[26] Similarly, the use of LiDFOB[20,27–29] is well documented in the literature. However, the remarkable performance achieved herein highlights

*Electrochemical Society Fellow.
[z]E-mail: croy@anl.gov

the importance of using an integrated approach to improve the performance of LMR cathodes in combination with graphite anodes. The results also demonstrate the feasibility of enhancing the performance of LMR cathodes for potential use in EVs. Herein, we focus on aluminum nitrate as the metal precursor in solution, as it was found to be quite effective under certain conditions as discussed below. Preliminary investigations (not presented here) suggest that other metal precursor may also be effective.

## Experimental

***Synthesis.***—Transition metal carbonate precursors ($Ni_{0.28}Mn_{0.53}Co_{0.19}CO_3$) were synthesized in a 4 L continuously stirred tank reactor. Aqueous solutions containing the stoichiometrically required 2M Ni-Mn-$CoSO_4$•$H_2O$, 2M $Na_2CO_3$, and 0.5M $NH_4OH$ were fed into the reactor at 50°C. The pH was kept constant with the $Na_2CO_3$ solution via a controller, and the reactor had a $N_2$ head to minimize unwanted oxidation of the product. After 24 hours, the reactor was drained, and the particles were washed before drying at 120°C under an inert gas (nitrogen).

After drying, the transition metal carbonate was mixed with lithium carbonate and fired at 900°C for 20 h in air to obtain a LLS baseline cathode powder targeting a "parent" LMR composition of, $0.25Li_2MnO_3$•$0.75LiMn_{0.375}Ni_{0.375}Co_{0.25}O_2$, containing, nominally, ∼6% spinel. The spinel component was incorporated by using less lithium than would normally be used to synthesize the parent LMR material in the lithiation/annealing process. More details of the synthesis can be found elsewhere.[7] The LLS baseline material was surface treated in an aqueous $Al(NO_3)_3 \cdot 9H_2O$ (∼0.5 wt%) solution, then dried at ∼100°C before heating to 200°C, 400°C, and 550°C in air. Samples are referred to in the text according to the annealing temperature of the Al surface treatment (i.e., Al_100°C, Al_200°C, Al_400°C, and Al_550°C).

***X-ray diffraction (XRD).***—High resolution synchrotron powder diffraction data were collected at the beamline 11-BM of the Advanced Photon Source, Argonne National Laboratory. The average wavelength was 0.41 Å. Discrete detectors covering an angular range from −6 to 16° 2θ were scanned over a 34° 2θ range, with data points collected every 0.001° 2θ and scan speed of 0.01°/s.

The 11-BM instrument uses X-ray optics with two platinum-striped mirrors and a double-crystal Si(111) monochromator, where the second crystal has an adjustable sagittal bend.[30] Ion chambers monitor incident flux. A vertical Huber 480 goniometer, equipped with a Heidenhain encoder, positions an analyzer system comprised of twelve perfect Si(111) analyzers and twelve Oxford-Danfysik $LaCl_3$ scintillators, with a spacing of 2° 2θ.[31] Analyzer orientation can be adjusted individually on two axes. A three-axis translation stage holds the sample mounting and allows it to be spun, typically at ∼5400 RPM (90 Hz). A Mitsubishi robotic arm is used to mount and dismount samples on the diffractometer. An Oxford Cryosystems Cryostream Plus device allows sample temperatures to be controlled over the range 80–500 K when the robot is used.

The diffractometer is controlled via EPICS.[32] Data are collected while continually scanning the diffractometer 2θ arm. A mixture of NIST standard reference materials, Si (SRM 640c) and $Al_2O_3$ (SRM 676) is used to calibrate the instrument, where the Si lattice constant determines the wavelength for each detector. Corrections are applied for detector sensitivity, 2θ offset, small differences in wavelength between detectors, and the source intensity, as noted by the ion chamber before merging the data into a single set of intensities evenly spaced in 2θ.

***Scanning electron microscopy (SEM) and energy-dispersive X-ray spectroscopy (EDX).***—The morphologies of the material were investigated by SEM and EDX spectroscopy using a Hitachi S-4700-II microscope in the Electron Microscopy Center, Argonne National Laboratory.

***X-ray photoelectron spectroscopy (XPS).***—XPS on pristine powders was performed with a Thermo Scientific Model K-Alpha XPS instrument. The instrument uses micro-focused, monochromatic Al $K_\alpha$ X-rays (1486.6 eV) which can be focused to a range of spot sizes from 30 to 400 μm. Most samples are analyzed with a 400-μm X-ray spot size to produce the maximum signal and to obtain an average surface composition over the largest possible area. The instrument has a hemispherical electron energy analyzer equipped with a 128 multi-channel electron detection system. For non-conducting samples, surface charging is avoided by using an integral charge compensation system consisting of low energy electrons and low energy Ar ions. The base pressure in the analysis chamber is typically $2 \times 10^{-9}$ mbar or lower. LLS powder samples were dispersed onto double-sided tape affixed to glass slides. Sufficient powder was used to completely hide the mounting tape. Because glass slides were used for sample mounting, the charge compensation system was used during data collection. Wide energy range survey spectra (0−1350 eV) were acquired for qualitative and quantitative analysis using an analyzer pass energy of 200 eV and an energy step size of 1 eV. Chemical bonding of the identified elements was assessed by collecting core level spectra over a narrow energy range using an analyzer pass energy of 50 eV and step size of 0.1 eV. Data were collected and processed with the Thermo Scientific Avantage XPS software package (v 4.61). When necessary, spectra were charge corrected with the C 1s core level peak set to 284.6 eV.

XPS measurements of the washed and harvested cathodes were performed in a PHI 5000 VersaProbe II system from Physical Electronics. The system was attached to the Ar-atmosphere glovebox, and the samples were inserted into the XPS analysis chamber through the glovebox without exposure to ambient air. The spectra were obtained by using an Al Kα radiation ($h\upsilon = 1486.6$ eV) beam (100 μm, 25 W), with Ar+ and electron beam sample neutralization, in Fixed Analyzer Transmission mode. The electron energy analyzer was operated at pass energy of 23.50 eV for high resolution spectra and 117.4 eV for all the survey scans. The base pressure is typically $\sim 2 \times 10^{-8}$ torr or lower in the analysis chamber. A step size of 0.02 eV was employed, and each peak was scanned for 50 times. To compensate for the effects of surface charging, all core-level spectra were referenced to the C1s hydrocarbon peak at 284.8 eV. Shirley background subtraction and fitting to multiple Gaussian-Lorentz peaks were performed on all spectra using the Multipack software from Physical Electronics.

***Transmission electron microscopy (TEM).***—The microstructures of the cathode material were investigated by transmission electron microscopy (TEM) at 200keV using a FEI Tecnai F20ST TEM. The compositions of the material were analyzed by scanning transmission electron microscopy (STEM) and energy dispersive X-ray spectrometer (EDX) at 200keV using a FEI Talos F200X TEM/STEM with a SuperX EDX system, allowing fast and precise elemental mapping. Both tools are provided by the Center for Nanoscale Materials, Argonne National Laboratory.

***Electrochemical characterization.***—Electrode laminates were prepared by coating aluminum foil with a slurry prepared with 84 wt% active material, 8 wt% Super P carbon, and 8 wt% polyvinylidene fluoride (PVDF) binder. Electrode loadings were maintained at $\sim 7$ mg·cm$^{-2}$. The cathode was cycled in cells against lithium and graphite anodes. A negative to positive electrode capacity ratio of ∼1.10 was targeted when cycled against graphite. Gen 2 electrolyte [1.2 M $LiPF_6$ in a 3:7 mixture of ethylene carbonate (EC) and ethyl methyl carbonate (EMC)] was used as the baseline electrolyte. All tests were done in temperature-controlled ovens held at 30°C.

## Results and Discussion

***TEM/STEM-EDX analysis.***—Initial characterization of the untreated LLS baseline electrode through XRD (Figure S1) revealed the presence of the dominant layered phases, $Li_2MnO_3$ (C2/m) and $LiNMCO_2$ (R-3m). Figure 1a shows a high-resolution TEM image of the Al_100°C sample. Information regarding the local structure of the

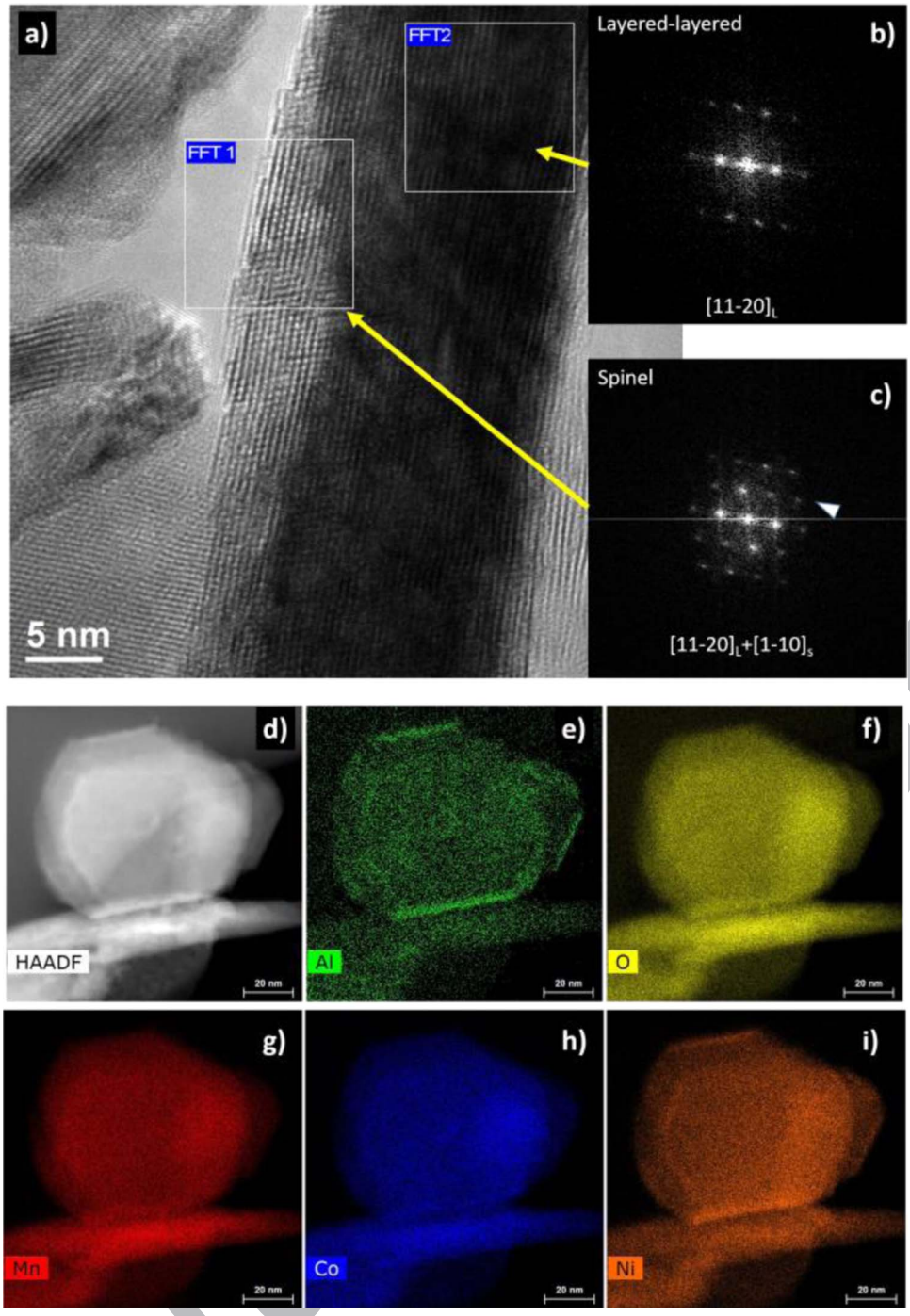


**Figure 1.** All images are of Al_100°C sample: (a) high-resolution TEM image and (b-c) Fast-Fourier Transform of regions FFT1 and FFT2 verifying the presence of both layered-layered and spinel domains within the same particle. (d) Z-contrast image and (e-i) STEM-EDX mapping showing the distribution of (e) Al, (f) O, (g) Mn, (h) Co, and (i) Ni on a single particle.

two boxed regions in Figure 1a is shown in the Fast Fourier Transforms (FFT) of Figures 1b and 1c and confirm the presence of the spinel and layered-layered domains within the same particle, as expected.[4] The presence of spinel and layered-layered domains was also confirmed on particles of the untreated LLS baseline (not shown). EDX mapping of the Al_100°C sample showed the presence of Al (Figure 1e) and the homogeneous distribution of transition metals (Figures 1g–1i).

***XPS analysis.—***Figures 2a–2b show the O 1s spectra collected on the untreated LLS baseline and the Al_100°C powders, respectively. The elemental surface compositions for both samples are shown in the table (see inset of Figure 2a). The peak centered at ~529.5 eV in both samples arises from the $O^{2-}$ anion in the bulk of the LLS lattice. A shoulder is also present in both samples on the high binding energy side of the lattice oxygen although the shoulder is less intense on the untreated baseline. A reasonable fit was achieved for the untreated baseline (Figure 2a) with an additional O peak assignment (O/C, ~531.5 eV) and the overlapping Na Auger. This peak can be associated with $Li_2CO_3$ on the surface as has been reported previously.[33] The O1s spectrum for the Al_100°C sample needed an additional O peak at ~532.5 eV for a reasonable fit (see Figure 2b). Due to the binding energy at which this peak appears, and the Al treatment the

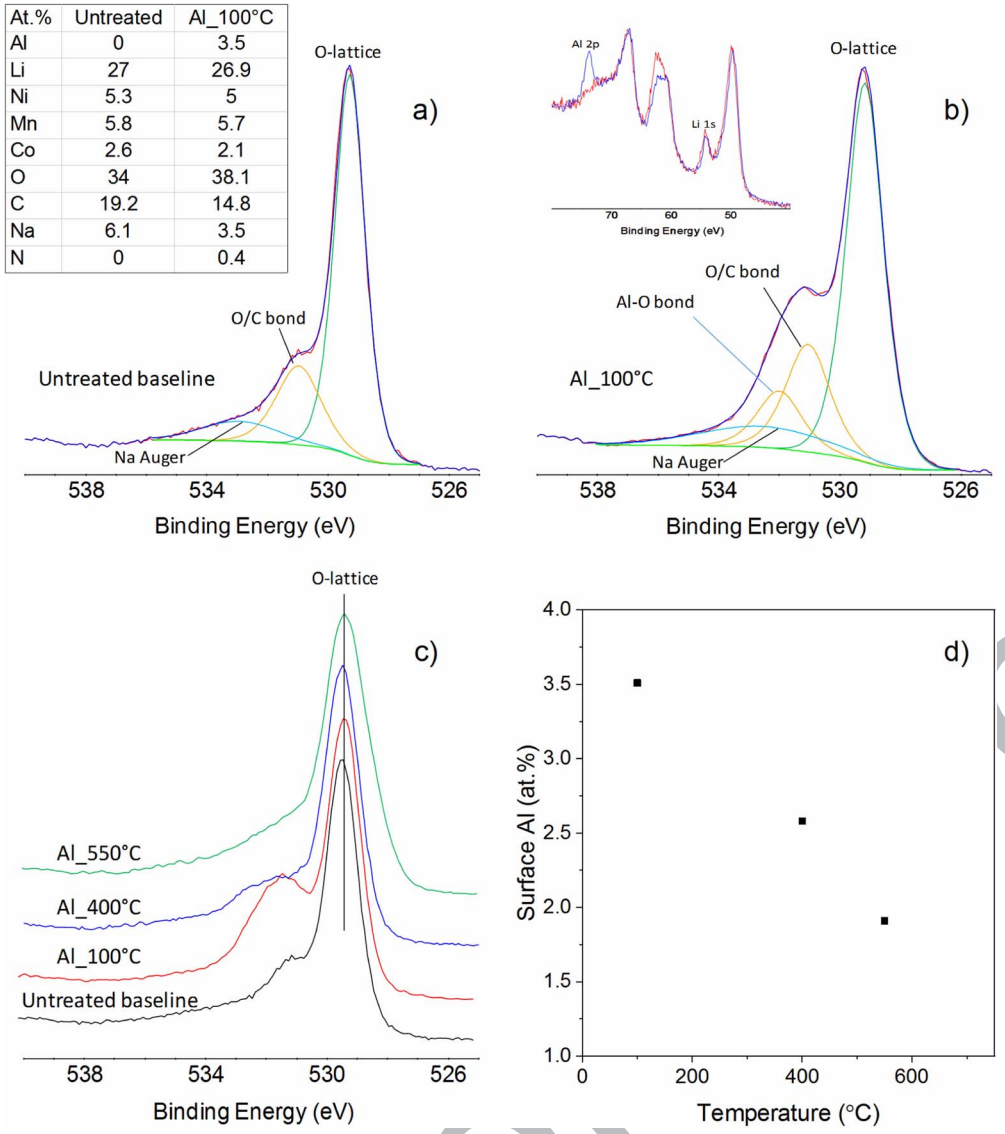


**Figure 2.** XPS results for O 1s core-level spectra of (a) untreated LLS baseline and (b) Al_100°C powders. The inset in (b) shows the Al 2p spectra of both samples, confirming the presence of Al in the treated sample. XPS results for (c) O 1s spectra showing changes of the high binding energy shoulder as a function of the post-treatment temperature. (d) Atomic percent aluminum on the surface of the treated samples as a function of processing temperature.

sample has undergone, this additional peak is assigned to O-Al bonds formed during the surface treatment. The ratio of the Al 2p peak (see inset of Figure 2b) and the O 1s peak at 532.5 eV gives a ratio (0.65) close to the ratio of Al:O in $Al_2O_3$ (0.67), though it is highly likely the surface treatment is at least partially hydroxylated (i.e. $Al_xO_yH_z$) due to the low processing temperature. Additionally, this new peak gradually loses intensity (see Figure 2c) as a function of processing temperature, coinciding with the decreasing surface-Al content (Figure 2d), and suggests a migration of Al from the surface into the bulk of the cathode.

***Cycle life and rate testing vs. $Li^+/Li^0$.***—Figure 3a shows how the processing temperature used *after* the Al surface-treatment affected the cycle life. The cycling protocol used to test the cycle life (Figure 3a) consisted of an activation cycle between 4.6–2.0 V (vs. $Li^+/Li^0$) followed by cycling between 4.45–2.5 V for all other cycles. Each sample in Figure 3a delivered similar capacity (~205 ± 5 mAh/g) for the 2nd cycle. The untreated LLS baseline lost ~8% of the initial capacity after 50 cycles while Al_100°C lost only 2%, delivering ~200 mAh/g after 50 cycles. Interestingly, the cycle life appears to degrade systematically with increasing processing temperature as the Al_550°C showed no improvement in cycle life compared to the untreated LLS baseline.

Figure 3b shows how the processing temperature affected the rate performance of the samples. The cycling protocol used the same activation cycle (4.6–2.0 V) as the cycle life testing followed by continuous cycling between 4.45–2.5 V. All charging was carried out at 15 mA/g followed by discharge currents between 15–1500 mA/g, as labeled in Figure 3b. The data shown are reported as a percentage of the capacity delivered on the 5th cycle discharge. The Al_550°C sample delivered ~200 mAh/g on the 5th cycle discharge. All other samples delivered ~205 mAh/g. At low currents (15–150 mA/g), very little difference was observed between any of the samples, treated or untreated, as each delivered very similar capacities. A difference in performance between the samples was observed as the current increased to 300 mA/g, with the Al_100°C and Al_200°C samples delivering similar capacities while also outperforming all other samples. In general, superior rate capability was demonstrated by the samples processed at a lower temperature, where the Al_100°C retained ~75% of its initial capacity at a discharge current of 1500 mA/g, compared to < 20% for the Al_550°C. An example of the standard deviation experienced by repeat cells is shown in Supplementary Figure S2.

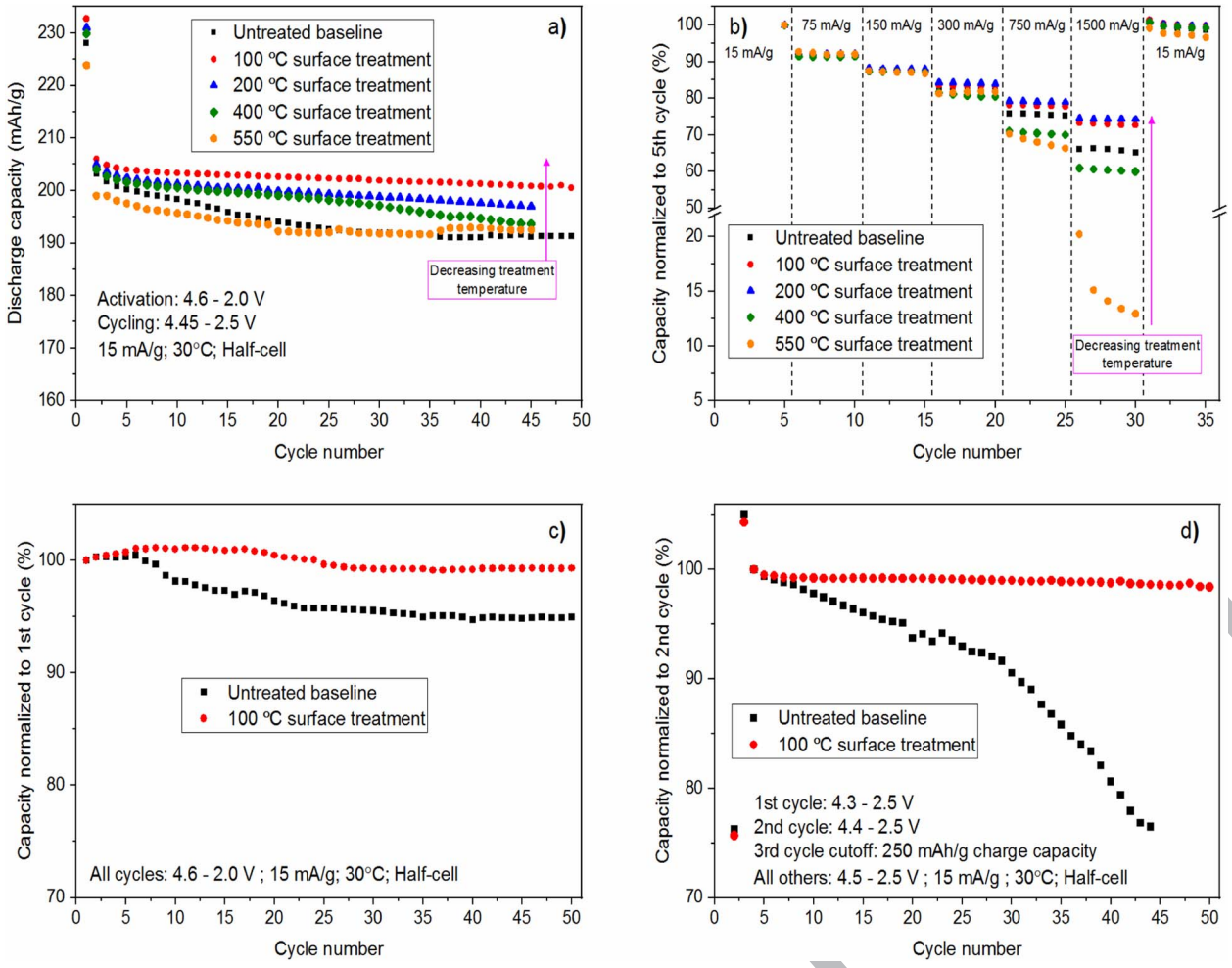


**Figure 3.** All electrochemical data of the cathodes were collected vs. a metallic lithium anode ($Li^+/Li^0$). The details for each protocol are shown in each of the figures. (a) Discharge capacity as a function of cycle number for the untreated LLS baseline and samples treated with $Al(NO_3)_3 \cdot 9H_2O$ and heated to the various temperatures shown. (b) Percent capacity (normalized to the 5th cycle ~200 mAh/g) delivered as a function of the discharge current. A 15 mA/g charging current was used for all cycles, followed by the various discharge currents shown. (c-d) Discharge capacity as a function of cycle number for the untreated LLS baseline and Al_100°C when (c) all voltage profiles are between 4.6–2.0 V and (d) the upper cutoff voltage increased from the initial value (4.3 V) to 4.5 V during initial cycles. A capacity of 250 mAh/g was used as the cutoff for the third cycle; all other cycling was carried out at 4.5–2.5 V (vs. $Li^+/Li^0$).

Further testing was carried out on the LLS baseline and Al_100°C samples with two additional protocols to determine if the performance of the treated sample would be similar under more aggressive cycling. Figure 3c shows the cycle life performance of both samples when cycled continuously between 4.6–2.0 V. The Al_100°C sample exhibited higher capacity retention compared to the LLS baseline (>99% vs. ~95%) even when exposed to the higher voltage cutoff. The data in Figure 3d were collected with a different cycling protocol. The upper voltage cutoff was incrementally increased over the first two cycles (i.e., 4.3 V to 4.4 V) while the lower voltage cutoff (2.5 V) remained the same. The 3rd cycle charge was capacity limited to 250 mAh/g instead of using a voltage cutoff. All other cycles were carried out between 4.5–2.5 V. As seen in the figure, the untreated LLS baseline lost 20% of the original capacity within the first 40 cycles. In contrast, the Al_100°C sample delivered >99% of its original capacity even after 50 cycles, providing further evidence of a more stable cathode for the sample treated at 100°C.

***Electrochemical impedance spectroscopy (EIS).—***The modified properties (i.e., improved capacity retention and rate performance, Figure 3) of the Al_100°C are, at least partially, related to the reduction in overpotential (represented by the green striped pattern for the 51st cycle in Figure 4a) observed during charge/discharge when compared to the untreated LLS baseline. The *total* overpotential has multiple contributions (ohmic, activation, and concentration),[34] which are related to the various internal processes that occur during cycling. It is difficult to determine the contribution from each type of overpotential by examining the charge/discharge curve shown in Figure 4a. In this regard, EIS is useful because it offers the ability to resolve contributions from the various types of overpotential.

The most common mode of representing EIS data is the Nyquist plot because it offers an easy way to observe changes in impedance between two different samples with similar aging or at *different* stages of the aging process for the *same* sample. Figure 4b is an illustration of a typical Nyquist plot showing how the impedance response to the frequency of the input can be separated into three distinct regions (dashed lines) associated with each type of overpotential loss. Each of the overpotential types can be categorized by their respective time constants (i.e., how fast the response occurs after the load is applied to the cell), and possible mechanisms that contribute to each type are listed below along with representations in Figure 4b:

• *Ohmic overpotential* occurs at very short times (or high frequencies), and contributions to this type of resistance/impedance include: ionic conductivity of the electrolyte; electronic conductivity of current collectors, carbon black, and active materials in the electrode; and contact resistance between active materials (anode or cathode) and current collectors or particle/particle contact.[35] Point A in

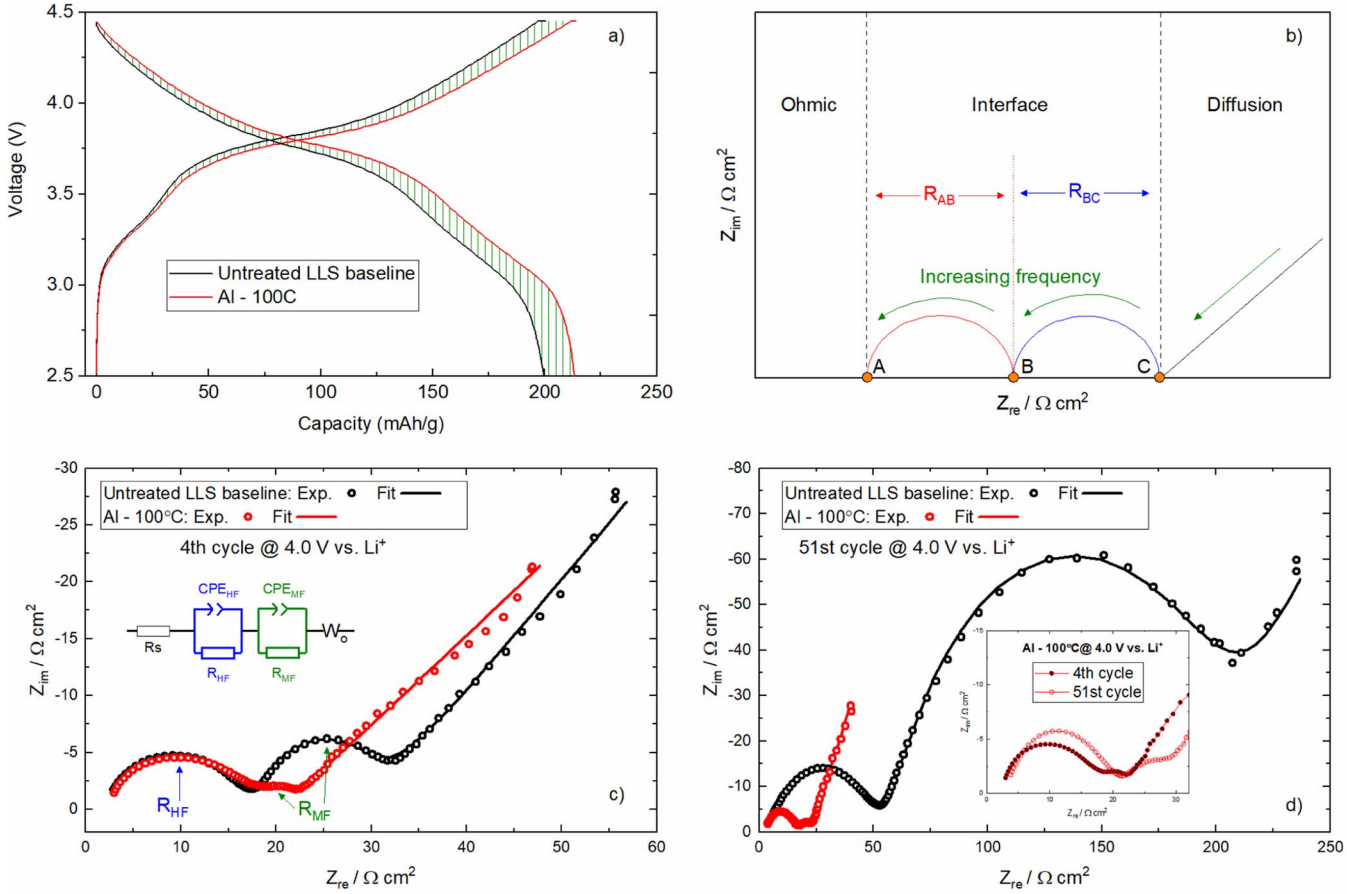


**Figure 4.** (a) Voltage profile of the untreated LLS baseline and Al_100°C samples after 50 cycles. The green pattern represents the overpotential difference between the two samples. (b) Schematic of a typical Nyquist plot obtained from EIS data collected on a lithium-ion cell. EIS data collected at room temperature on the untreated LLS baseline and Al_100°C at 4.0 V vs. $Li^+/Li^0$ (2032 coin-cell format) during the (c) 4$^{th}$ cycle and (d) 51$^{st}$ cycle. The inset of (d) is a comparison of the 4$^{th}$ and 51$^{st}$ cycle of the Al_100°C sample.

Figure 4b represents the ohmic overpotential and is expected to remain constant over the course of testing.[36]

• *Activation overpotential* is related to charge transfer reactions that occur at interfaces (i.e. anode/electrolyte, anode/current collector, cathode/electrolyte, and cathode/current collector). This polarization includes charge transfer to/from any electrolyte decomposition products found on the surface of the anode (solid-electrolyte interphase, SEI) or cathode (cathode-electrolyte interphase, CEI). Differences in EIS data between the treated and baseline samples in this study are expected to occur in this region. Generally, the Nyquist plot of LMR materials consists of two semi-circles ($R_{AB}$ and $R_{BC}$) in this region, as shown in Figure 4b. *Each* "perfect" (i.e. not depressed or flat) semi-circle corresponds to a *single* process requiring a separate activation energy for charge transfer to occur. The physical interpretation of each of the semi-circles is varied in the literature and will be addressed further below.

• *Concentration overpotential* occurs when the diffusion of lithium (generally considered as bulk diffusion) is hindered because a concentration gradient has emerged at an interface.[35,36] This type of overpotential loss is observed as a sloping line at low frequencies in the Nyquist plot (Figure 4b).

EIS data were collected on the untreated LLS baseline and Al_100°C samples at various stages of cycle life for comparison. The impedance of each sample was collected at low (3.5 V), mid (4.0 V), and high (4.5 V) states of charge (SOCs) during the 4$^{th}$ and 51$^{st}$ cycles. The testing was carried out in coin-cells with lithium metal as the anode. The complete results are shown in Figure S3. Following are some general observations that apply to both samples, surface-treated and baseline. The ohmic contribution to the impedance (~3 Ω cm$^2$) was similar in both samples, as expected, and did not change throughout testing. In addition, both samples exhibited two semi-circles (high frequency, $R_{HF}$; mid frequency, $R_{MF}$) at all SOCs and at different stages of cycling (4$^{th}$ and 51$^{st}$ cycle). The SOC did *not* have an effect on $R_{HF}$, but $R_{MF}$ was highly dependent on SOC (see Figure S3). The impedance associated with $R_{MF}$ was smallest at the mid (4.0 V) SOC whereas it was larger when the cell was at low (3.5 V) and high (4.5 V) SOCs. A similar trend was observed on discharge (not shown). The impedance changes associated with $R_{MF}$ as a function of SOC are generally expected, as emphasized by recent work on both layered ($LiCoO_2$)[38] and LMR[39] cathodes.

Figures 4c and 4d compare the results of the 4$^{th}$ and 51$^{st}$ cycle, respectively, at mid SOCs (4.0 V), which are representative of the differences observed between the two samples. The EIS spectra were analyzed using the equivalent circuit shown in Figure 4c. The electrolyte resistance was modeled using a resistor. Each semi-circle was modeled using a constant phase element and resistor in parallel. As shown in Figure 4c, the impedance associated with $R_{HF}$ is similar (~14.5 Ω cm$^2$) for both samples at beginning of life while the impedance associated with $R_{MF}$ is already several times greater in the untreated baseline (~15 Ω cm$^2$) compared to Al_100°C (~4 Ω cm$^2$). At the end of testing (Figure 4d), both $R_{HF}$ and $R_{MF}$ increased significantly in the untreated baseline (~49 Ω cm$^2$ and >150 Ω cm$^2$) while *minimal* changes were observed in Al_100°C (~16 Ω cm$^2$ and ~6 Ω cm$^2$; inset of Figure 4d).

The results presented in Figures 4c and 4d are more useful accompanied by a physical model to understand the results. Therefore, following is a brief description of recent works in the literature that

provide the framework of our interpretation. Before doing so, it is helpful to remember that the internal processes within the cell require transfer of *both* lithium ions and electrons to occur. This means that the impedance related to each process will vary if the availability of *either* lithium or electrons deviates in some way, such as changes in mass transport or charge transfer.[40]

A numerical model recently developed for understanding EIS data shows that $R_{HF}$ increases when the conductivity of the bulk electrolyte is decreased (i.e., depletion of available lithium).[41] This explanation is supported by experimental work on $LiCoO_2$ that showed the same result (i.e., electrolyte conductivity can change the size of $R_{HF}$).[38] Furthermore, $R_{HF}$ can *also* be altered by manipulating the *electronic* resistance by preparing electrodes with different compression pressures. This resistance is believed to affect the availability of electrons by changing particle/particle contact.[38] Consequently, the impedance associated with $R_{HF}$ was assigned to the adsorption/desorption of lithium on the surface of the composite electrode.[38] We adopt this interpretation of $R_{HF}$ for this work.

The interpretations of $R_{MF}$ found in the literature include both charge transfer and the impedance associated with the CEI. As mentioned above, each semi-circle is related to a *single process/mechanism* requiring one activation energy. Tatara et al. recently showed that the activation energy for $R_{MF}$ is comparable to charge transfer reactions, where desolvation/solvation of lithium is the rate determining step, and lithium ion conduction in inorganic solid electrolytes (i.e., CEI).[38] Therefore, it seems plausible that both interpretations for $R_{MF}$, charge transfer and CEI impedance, are related to a single *process* (i.e., absorption). We note that a number of factors can affect the activation energy (i.e., impedance) of the process but adopt the assignment of $R_{MF}$ as the absorption of lithium ions into the bulk of the oxide.

Returning to the results presented in Figures 4c and 4d we note that at the beginning of life, adsorption $R_{HF}$ is similar in both samples while absorption $R_{MF}$ is already several times greater in the untreated baseline. At the end of testing (Figure 4d), both $R_{HF}$ and $R_{MF}$ increased significantly in the untreated baseline while minimal changes were observed in Al_100°C (inset of Figure 4d). There may be several contributing factors for the higher impedance in the untreated baseline. For example, if the concentration of dissolved Mn in the electrolyte is different for the untreated baseline and Al_100°C cells, this could lead to the observed differences in impedance.[42] Nevertheless, it is clear that the changes in impedance between the two samples was brought about by changes to the cathode surface properties after treatment. Therefore, we might expect the properties (i.e. thickness, composition, etc.) of the CEI for each sample is also different.

***Analysis of CEI by X-ray photoelectron spectroscopy (XPS).—*** Detailed analyses of the surface of the untreated LLS baseline and the Al_100°C samples were carried out with XPS to examine the differences in the CEI between the two samples. Figure 5 shows spectra (C 1s, O 1s, F 1s, and P 2p) collected on electrodes after 50 cycles (vs. $Li^+/Li^0$). The C 1s spectrum (Figure 5a) was fit using five signals, and the various species[43] associated with each of the signals are labeled in the figure. The spectra for both samples are similar but do show small differences. Most notable is the slight increase in signal from carbon atoms singly bound to oxygen in C-O-C=O (esters; binding energy of ~286.9 eV) in the Al_100°C sample. The O 1s spectrum (Figure 5b) shows this increase more clearly, also revealing a higher percentage of oxygen atoms singly bound to carbon in esters (C-O-C=O) for the Al_100°C sample. Interestingly, larger contributions from O near the same binding energy (~534 eV) have been correlated with improved electrochemical performance by the use of fluorinated electrolytes as well.[44]

Figures 5c and 5d show that a higher quantity of fluorinated species is present on the untreated LLS baseline vs. the Al_100°C. For instance, the fluorine peak at ~688 eV (Figure 5c) is associated with PVDF and is similar in both samples, whereas the *ratio* of the peaks at 686 and 688 eV is almost 2x larger in the untreated baseline. The peak at 686 eV is associated with $Li_xPO_yF_z$,[45] which suggests that more decomposition of $LiPF_6$ salt, via parasitic side reactions,[46] has occurred for the untreated baseline cell. Additionally, a comparison of P 2p spectra for both samples (Figure 5d) also suggests that the CEI of the Al_100°C sample may be relatively "oxygen-rich" while that of the untreated baseline may be slightly more "fluorine-rich". For example, although the P 2p spectra of both samples lie between 135 and 136 eV, there is a minor shift to higher binding energy for the untreated baseline. Peaks in this region are associated with several phases that differ in fluorine and oxygen content ($Li_xPO_{y-1}F_{z+1}$, $Li_xPO_yF_z$, and $Li_xPO_y$) where the binding energy increases, as in the case of the untreated baseline, when the phase contains greater amounts of fluorine.[43] The reasons the Al_100°C treatment promotes these changes specifically in the CEI are unknown. However, these data support the interpretation of the impedance data above and confirm that the low-temperature aluminum treatment does, in fact, change the nature of the CEI that is formed over cycling.

***Electrolyte optimization by use of lithium difluoro(oxalate) borate (LiDFOB).—*** As mentioned above, capacity fade in cells utilizing graphite anodes can originate from side reactions at the graphite surface that result in loss of active lithium.[21] Recent work has also reiterated that the explicit dissolution and subsequent deposition of Mn on



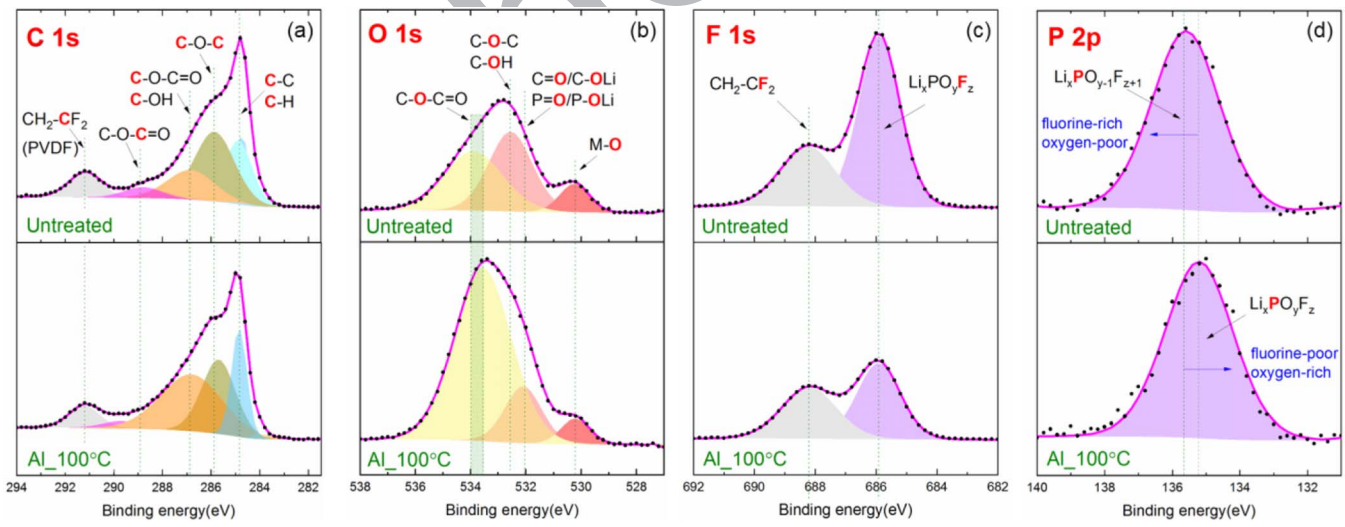


**Figure 5.** X-ray photoelectron spectra of (a) C 1s, (b) O 1s, (c) F 1s, and (d) P 2p for untreated LLS baseline (top) and Al_100°C (bottom) electrodes after 50 cycles (vs. $Li^+/Li^0$).

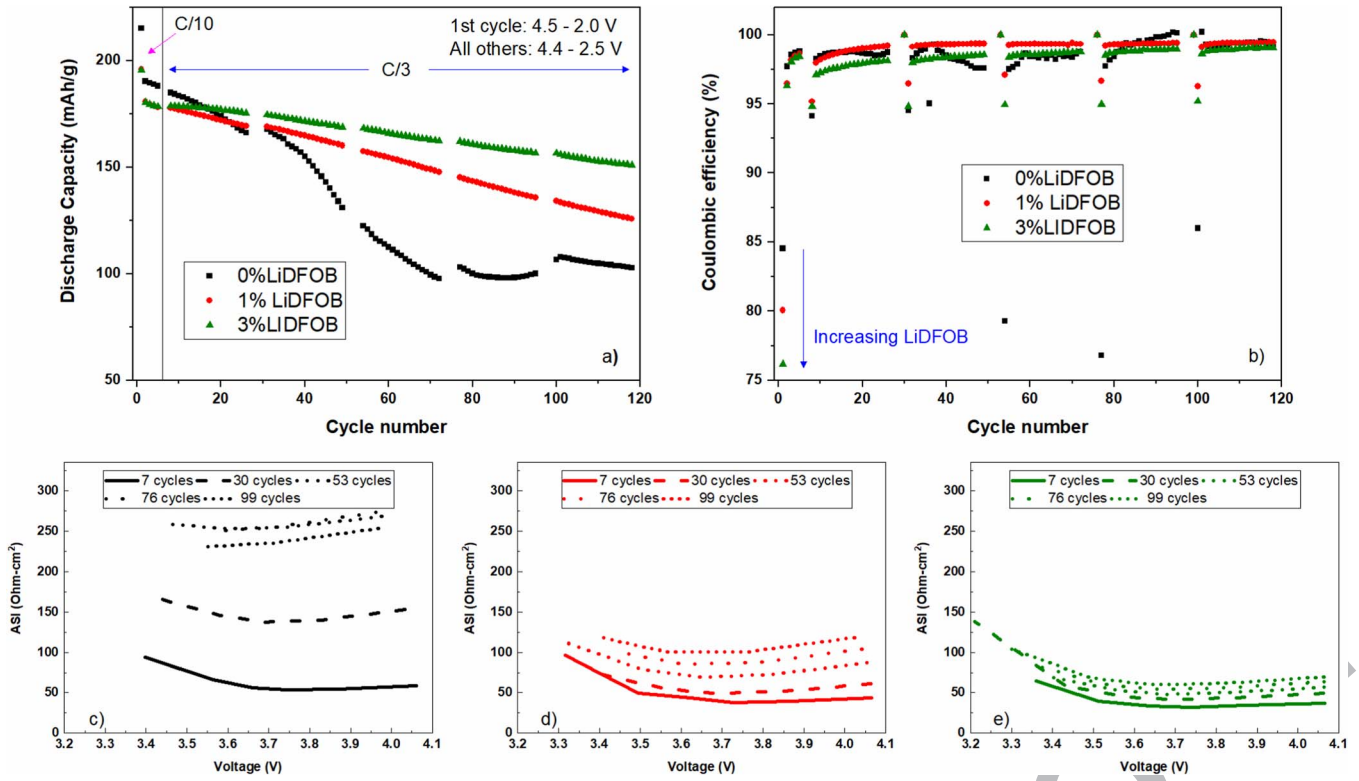


**Figure 6.** Electrochemical data for three full-cell (vs. graphite) systems containing the same untreated LLS cathode using different concentrations (0, 1, and 3 wt%) of LiDFOB additive in the electrolyte. (a) Cycle life performance. The LLS cathode was activated between 4.5–2.0 V (vs. graphite) then cycled between 4.4–2.5 V for all other cycles; all cycles were carried out at 30°C. The current used for each cycle is indicated in the figure. (b) Coulombic efficiency of each system as a function of cycle number. (c-e) Area-specific-impedance (ASI) collected on full-cells shown in (a) with different concentrations of LiDFOB in the electrolyte: (c) 0%, (d) 1 wt%, and (e) 3 wt%.

graphite is highly correlated with lithium "trapping" in the SEI layer.[47] It is therefore expected that cells containing Mn-rich LMR cathodes (with no surface treatment), when paired with graphite anodes, may experience high levels of capacity fade due to Mn dissolution when cycled to high cutoff voltages. The protocol used in Figure 6 has five formation cycles. The first cycle is carried out between 4.5–2.0 V (C/10) to allow access to the additional capacity available in LMR cathodes when "activation" occurs. The next four formation cycles were carried out between 4.4–2.5 V (C/10). All subsequnt cycles in the protocol are carried out between 4.4–2.5 V (C/3). The cycles where no data is shown are used to collected area-specific-impedance data, which will be addressed in more detail below. This protocol is intended to exacerbate cathode surface degradation (e.g., metal dissolution) and thereby accelerate the mechanisms of capacity fade by using 3-hour holds at the top of each "high-voltage" charge (4.4 V) during ~120 aging cycles.[48] Figure 6a shows that untreated baseline LLS//graphite cells do indeed experience a high degree of capacity fade, reaching end of life (~20% capacity loss) in < 50 cycles, under such an aggressive protocol. Both electrodes from the LLS//graphite cells were harvested after full-cell cycling was complete and rate tested vs. $Li^+/Li^0$. The harvested cathode showed little difference (Figure S4a) with respect to capacity and retention when compared with a fresh cathode throughout the test. On the other hand, the harvested anode exhibited lower initial capacity and quickly deteriorated (Figure S4b). EDX analysis was carried out and will be shown further belowvels of Mn on the anode, as expected.

Among the approaches to lessen the dissolution of transition metals (TM), the use of electrolyte additives provides a convenient method to form an effective surface film on the cathode particles in-situ (i.e., during cycling) that can alleviate unwanted secondary reactions. LiDFOB has been used extensively in the literature on Mn-rich cathode materials such as LMR[20,27,28] and spinel.[29] The use of LiDFOB in full-cell configurations is considered multifunctional, as it is proposed to provide interfacial stability on both the anode and cathode by limiting lithium loss and minimizing impedance rise, respectively.[20,27,49] Figure 6a shows that the cycle life of the untreated, LLS baseline cathode is improved (Figure 6a) to a certain degree when utilizing LiDFOB as an additive (1 and 3 wt% in the electrolyte) with some sacrifice in first cycle efficiency (FCE). Although the FCE (Figure 6b) of the untreated baseline with 0% LiDFOB was the highest, it exhibited a higher degree of instability, suggesting high levels of unwanted secondary reactions. The coulombic efficiency of the system was stabilized significantly by the addition of 1 wt% LiDFOB when compared to the system without additive. The coulombic efficiency was also stable when 3 wt% LiDFOB was used. However, increasing amounts of the additive came at the cost of lower coulombic efficiencies during extended cycling. Note that the lower FCE for systems using LiDFOB (vs. electrolyte with no additive) has been attributed to higher lithium consumption during the formation of the SEI.[27] The data here reiterate that while LiDFOB as an additive shows some promise with respect to Mn-rich cathodes, high amounts are needed for significant improvements, which come at the cost of lower efficiencies.

Lastly, the ASI of the baseline (0% LiDFOB; Figure 6c), 1 wt% (Figure 6d) and 3 wt% (Figure 6e) was collected as a function of cycle number (shown as breaks in the cycling data, Figures 6a and 6b) using the protocol described in Ref. 48. Briefly, each cell is charged to the same upper cutoff voltage (4.4 V) at C/3 and allowed to rest for 1 hour. What follows is a series of discharge and charge pulses applied at different states of charge (SOC) while the voltage and current are monitored. This allows for the calculation of the ASI by using the differences in voltage and current at the start and end-point of each pulse. Figures 6c-e show the ASI for the *discharge* cycle as a function of cycle number. In general, the ASI increases with increasing cycle number for each of the samples. The extent of the increase correlates well with the amount of LiDFOB in the electrolyte, with less

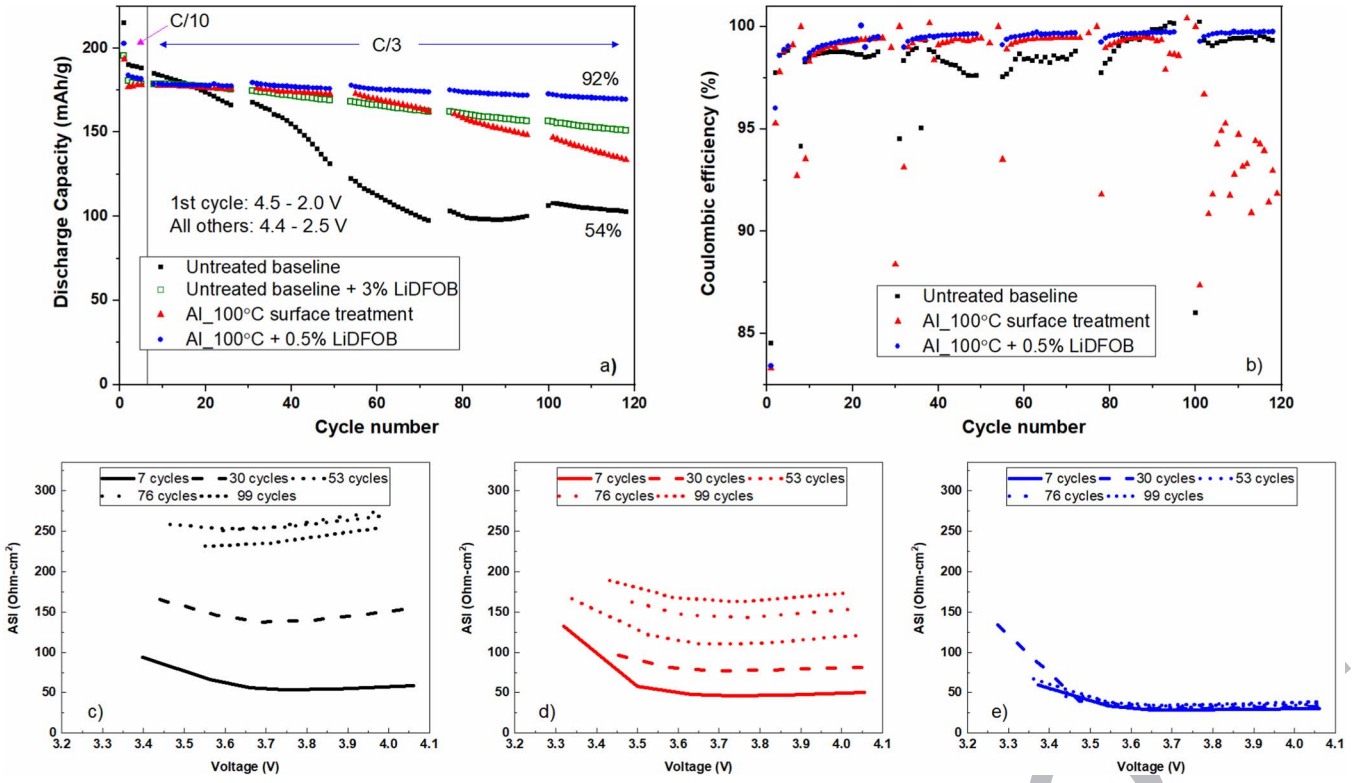


**Figure 7.** Electrochemical data for untreated LLS baseline//graphite and Al_100C//graphite cells with and without LiDFOB. (a) Cycle life performance. Each cell was activated between 4.5–2.0 V (vs. graphite) then cycled between 4.4–2.5 for all other cycles; all cycles were carried out at 30°C. The current used for each cycle is indicated in the figure. (b) Coulombic efficiency of each system as a function of cycle number. (c-e) Area-specific-impedance collected on full-cells shown in (a): (c) untreated LLS baseline//graphite in Gen 2, (d) Al_100C//graphite in Gen 2, and (e) LiDFOB-Al//graphite.

impedance rise occurring when *higher* concentrations of the additive are used.

***Full-cell validation of surface-treated cathode.—***The Al_100°C sample was also tested in a full-cell configuration (vs. graphite) under the same protocol (Figure 7a) described above, with and without the addition of 0.5 wt% LiDFOB (referenced hereafter as LiDFOB-Al). The initial capacity was slightly lower for the Al_100°C (~195 mAh/g) and LiDFOB-Al (~205 mAh/g) when compared to the untreated LLS baseline (~215 mAh/g). The initial capacity delivered with 3 wt% LiDFOB (~200 mAh/g) is also shown in Figure 7a for reference. Due to the significant capacity fade of the untreated baseline, the Al_100°C and LiDFOB-Al systems deliver a higher discharge capacity by the 20$^{th}$ cycle. Upon further cycling the capacity fade increases greatly for Al_100°C near the 50$^{th}$ cycle, so much that by the end of the cycling protocol the Al_100°C shows only a slight improvement over the untreated baseline. On the other hand, LiDFOB-Al exhibited extraordinary capacity retention, even under this harsh, high voltage protocol, as it delivered 92% of the original capacity after ~120 cycles.

Figure 7b shows the coulombic efficiency as a function of cycle number for the untreated baseline, the Al_100°C, and the LiDFOB-Al. The FCE for the Al_100°C and the LiDFOB-Al samples were about equal (~83%) to that of the untreated baseline (~84%). Yet, upon extended cycling the coulombic efficiency of the Al_100°C was higher compared to that of the untreated baseline, and the combination of the surface treatment with the LiDFOB (i.e., LiDFOB-Al) exhibited the highest coulombic efficiency over the course of testing. In similar manner, the Al_100°C experienced less rise in impedance during cycling (Figure 7d) when compared to the untreated baseline (Figure 7c), while the combination of the low-temperature surface treatment and the use of a small amount of LiDFOB (i.e., LiDFOB-Al in Figure 7e) resulted in nominal rise in impedance over the life of the cell. The *combined* effect of the surface treatment and the electrolyte additive thus revealed a superior electrochemical performance than that with either treatment by itself.

The properties (composition, thickness, etc.) of the SEI have a significant impact on the long-term performance of metal-oxide//graphite cells, and small changes during formation processes can have a large impact on overall cell performance.[50] Figure 8a shows a 1$^{st}$-cycle dQ/dV comparison among each of the systems discussed thus far. For the untreated LLS baseline//graphite in Gen 2 electrolyte, a sharp peak near 3.0 V is apparent (Figure 8b). This peak is associated with the reduction of EC on graphite, the main SEI formation process, and is irreversible. The dQ/dV of the Al_100°C//graphite in the same Gen 2 electrolyte (Figure 8c), exhibits a peak near 2.4 V and a "muted" peak near 3.0 V, suggesting that the SEI formation processes of *both* electrode/electrolyte interphases (CEI/SEI) have been modified by the low temperature surface treatment. Since the surface treatment of the cathode was done at such a low-temperature (100°C), the Al phase on the surface might have dissolved into the electrolyte and acted as an additive. This possibility will be discussed in more detail below. With the addition of 0.5 wt% LiDFOB in the untreated LLS baseline//graphite cells, a peak near 2.1 V, associated with the reduction of LiDFOB, appears in the dQ/dV (Figure 8d). The reduction of LiDFOB occurs before the reduction of EC and is believed to improve the stability of the SEI and CEI by forming a robust passivation layer on graphite and reducing the dissolution of transition metals from the cathode.[20] Finally, the dQ/dV of the LiDFOB-Al//graphite cells (Figure 8e) reveals the presence of each passivating reaction (anode and/or cathode) when both strategies are used in combination. These small changes in dQ/dV combined with XPS (Figure 5) and the electrochemical results (Figure 7) suggest that the formation of the electrode/electrolyte interphases are modified greatly. Indeed, SEM images collected on the harvested anode from the LiDFOB-Al//graphite cell (Figure 9b) reveal that less electrolyte breakdown occurred, as the SEI appears thinner and the underlying graphite is still visible. Moreover, EDX analysis of the anode from a LiDFOB-

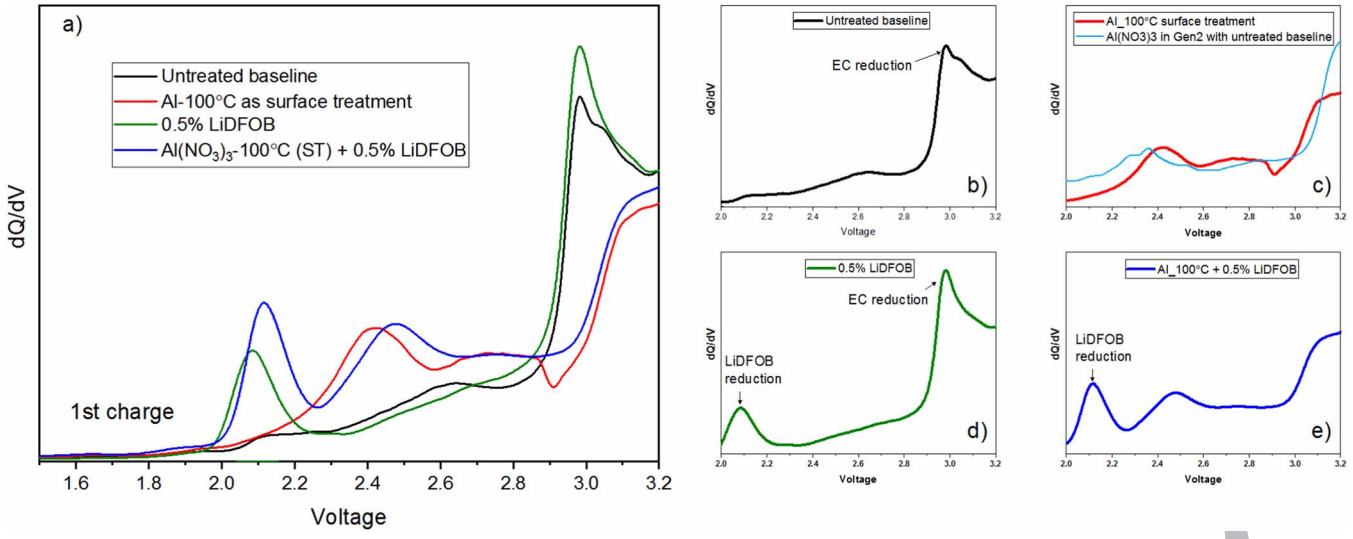


**Figure 8.** Comparison of dQ/dV (1st cycle charge only) for (a) various LLS//graphite cells with and without LiDFOB and/or surface treatment, (b) untreated LLS baseline//graphite in Gen 2, (c) Al_100°C//graphite in Gen 2, (d) untreated LLS baseline//graphite with 0.5 wt% LiDFOB, and (e) LiDFOB-Al//graphite.

Al//graphite cell showed no Mn present (Figure 9d), which is believed to be the main cause for the improved cycle life. Conversely, a thick SEI formed on the anode of the untreated LLS baseline//graphite without LiDFOB (Figure 9a) that revealed the presence of Mn (Figure 9c).

The question remains whether the Al phase achieved during the surface treatment dissolves in the electrolyte and acts as an additive due to the low-temperature used during the process. To test this hypothesis, the precursor ($Al(NO_3)_3 \bullet 9H_2O$) used for the surface treatment was dissolved in water and dried at 100°C to replicate the process used on Al_100°C. The "processed" aluminum nitrate (Al_addit) was then used as an additive for untreated LLS baseline//graphite cells. The dQ/dV of the first cycle charge is shown in Figure 8c along with the Al_100C revealing similarities and differences. For instance, the peak at ~2.4 V is slightly shifted to lower potential, and the peak at 3.0 V is not muted as in the Al_100°C (without additive) or LiDFOB-Al (Figure 8e). Furthermore, the overall electrochemical performance of the Al_addit is inferior to that of the Al_100°C (Figures 10a and 10b), in which the initial capacity and capacity retention are lower (Figure 10a). Likewise, the coulombic efficiency (Figure 10b) is lower, and the ASI (inset of Figure 10b) growth is higher for the Al_addit. These differences in the electrochemical behavior suggest that the



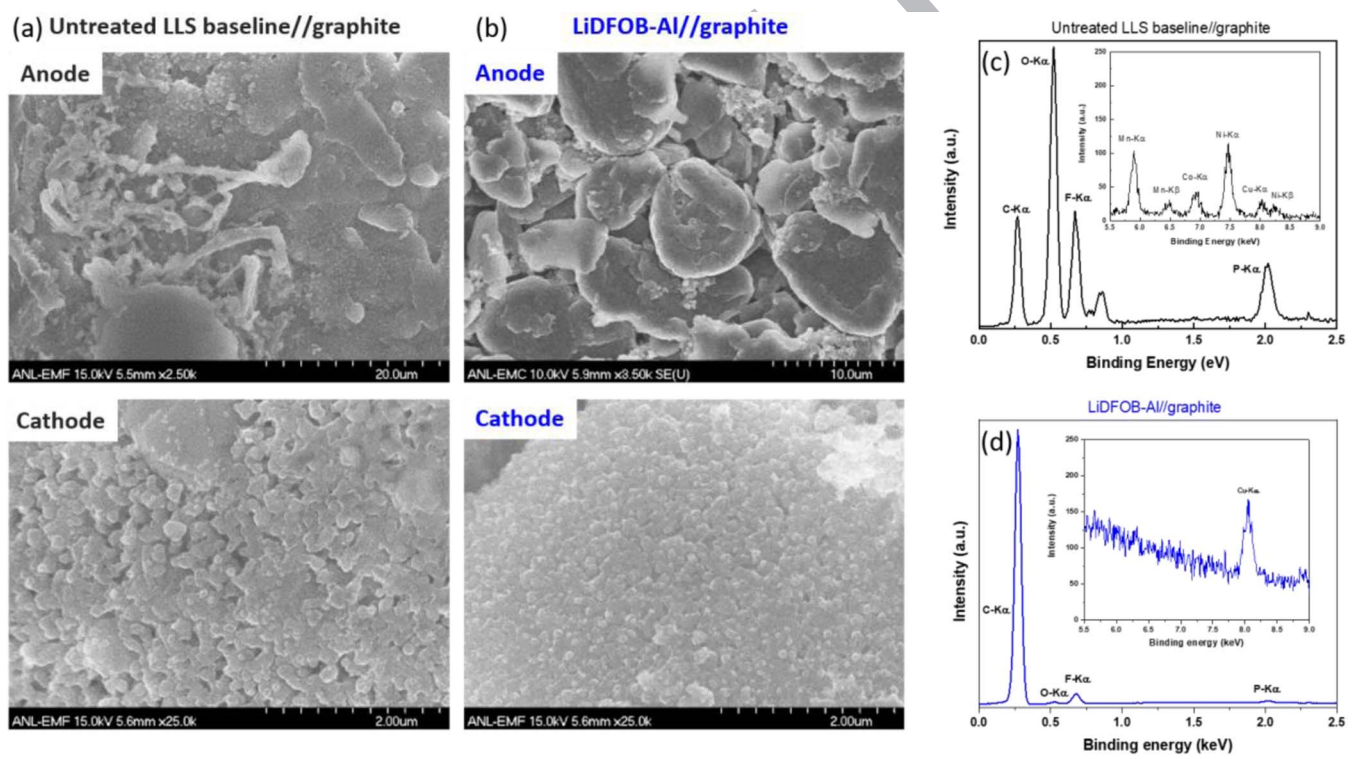


**Figure 9.** SEM of harvested anode and cathode from (a) untreated LLS baseline//graphite and (b) LiDFOB-Al//graphite cells. (c-d) EDX spectra collected on harvested anodes after ~120 cycles from (c) untreated LLS baseline//graphite and (d) LiDFOB-Al//graphite cells.

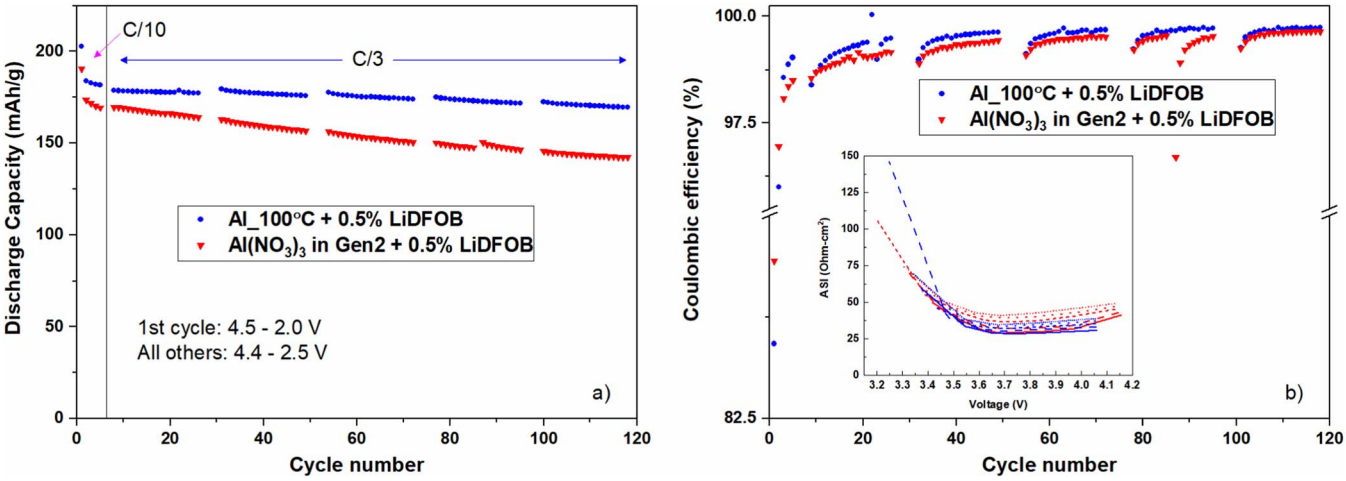


**Figure 10.** Electrochemical data for Al_100C//graphite and LLS//graphite cells with 0.5 wt% LiDFOB in Gen 2. $Al(NO_3)_3 \cdot 9H_2O$ was added as an electrolyte additive to the LLS//graphite cells. (a) Cycle life performance. Each cell was activated between 4.5–2.0 V (vs. graphite) then cycled between 4.4–2.5 for all other cycles; all cycles were carried out at 30°C. The current used for each cycle is indicated in the figure. (b) Coulombic efficiency of each system as a function of cycle number. (inset of b) Area-specific-impedance.

aluminum nitrate behaves differently when used as an additive instead of as a surface treatment.

## Conclusions

Herein, we demonstrated that a combined optimization strategy (both electrolyte additive and surface treatment) can greatly improve the performance of LMR cathodes. The use of a low-temperature surface treatment improved the capacity retention and rate performance of the baseline LLS cathode. The modified cathode showed improved impedance properties compared to that of the untreated LLS baseline. An analysis of the surface-treated cathode (after cycling) revealed the composition of the CEI was relatively oxygen-rich, while the untreated baseline was relatively fluorine-rich by comparison. The use of higher concentrations of LiDFOB in Gen 2 electrolyte provided some improvement to the capacity retention of untreated LLS baseline//graphite cells but at the cost of lower coulombic efficiency. The surface-treated cathode (Al_100C) exhibited only minimal improvements to the ASI and capacity retention compared to those of the untreated LLS baseline when cycled in full-cells. On the other hand, outstanding capacity retention (92%) and minimal impedance rise were achieved when the surface-treated cathode was used in combination with LiDFOB (0.5 wt%). The improved electrochemistry due to the combined approach is attributed to reduced Mn dissolution from the cathode and consequent deposition on the anode. The results detailed here provide a simple and scalable strategy for improving the performance of LMR-type cathode materials for use in industry-relevant cells.

## Acknowledgments

Support from the U. S. Department of Energy, Office of Energy Efficiency and Renewable Energy, in particular David Howell and Peter Faguy, is gratefully acknowledged. The submitted manuscript has been created by UChicago Argonne, LLC, Operator of Argonne National Laboratory ("Argonne"). Argonne, a U. S. Department of Energy Office of Science laboratory, is operated under Contract No. DE-AC02–06CH11357. The U. S. Government retains for itself, and others acting on its behalf, a paid-up, nonexclusive, irrevocable worldwide license in said article to reproduce, prepare derivative works, distribute copies to the public, and perform publicly and display publicly, by or on behalf of the Government. Use of the Advanced Photon Source at Argonne National Laboratory was supported by the U. S. Department of Energy, Office of Science, Office of Basic Energy Sciences, under Contract No. DE-AC02-06CH11357. Use of the Center for Nanoscale Materials, an Office of Science user facility, was supported by the U. S. Department of Energy, Office of Science, Office of Basic Energy Sciences, under Contract No. DE-AC02-06CH11357.

## ORCID

Arturo Gutierrez https://orcid.org/0000-0002-2899-3089

## References

1. Z. H. Lu, L. Y. Beaulieu, R. A. Donaberger, C. L. Thomas, and J. R. Dahn, *J. Electrochem. Soc.*, **149**, A778 (2002).
2. M. M. Thackeray, C. S. Johnson, J. T. Vaughey, N. Li, and S. A. Hackney, *J. Mater. Chem.*, **15**, 2257 (2005).
3. A. R. Armstrong, M. Holzapfel, P. Novak, C. Johnson, S.-H. Kang, M. Thackeray, and P. G. Bruce, *J. Am. Chem. Soc.*, **128**, 8694 (2006).
4. J. R. Croy, M. Balasubramanian, K. G. Gallagher, and A. K. Burrell, *Acc. Chem. Res.*, **48**, 2813 (2015).
5. S. Park, S. Kang, C. Johnson, K. Amine, and M. Thackeray, *Electrochem. Commun.*, **9**, 262 (2007).
6. D. Kim, G. Sandi, J. R. Croy, K. G. Gallagher, S. H. Kang, E. Lee, M. D. Slater, C. S. Johnson, and M. M. Thackeray, *J. Electrochem. Soc.*, **160**, A31 (2013).
7. B. R. Long, J. R. Croy, J. S. Park, J. G. Wen, D. J. Miller, and M. M. Thackeray, *J. Electrochem. Soc.*, **161**, A2160 (2014).
8. N. Tran, L. Croguennec, M. Menetrier, F. Weill, P. Biensan, C. Jordy, and C. Delmas, *Chem. Mater.*, **20**, 4815 (2008).
9. P. G. Bruce, S. A. Freunberger, L. J. Hardwick, and J. M. Tarascon, *Nat. Mater.*, **11** (2012). Q1
10. S. A. Freunberger, Y. H. Chen, Z. Q. Peng, J. M. Griffin, L. J. Hardwick, F. Barde, P. Novak, and P. G. Bruce, *J. Am. Chem. Soc.*, **133**, 8040 (2011).
11. J. Hong, H. D. Lim, M. Lee, S. W. Kim, H. Kim, S. T. Oh, G. C. Chung, and K. Kang, *Chem. Mater.*, **24**, 2692 (2012).
12. Q. Xia, X. Zhao, M. Xu, Z. Ding, J. Liu, L. Chen, D. G. Ivey, and W. Wei, *J. Mater. Chem. A*, **3**, 3995 (2015).
13. B. Song, C. Zhou, Y. Chen, Z. Liu, M. O. Lai, J. Xue, and L. Lu, *RSC Adv.*, **4**, 44244 (2014).
14. S.-H. Kang and M. M. Thackeray, *Electrochem. Commun.*, **11**, 748 (2009).
15. Z. Wang, E. Liu, C. He, C. Shi, J. Li, and N. Zhao, *J. Power Sources*, **236**, 25 (2013).
16. F. Wu, N. Li, Y. Su, H. Lu, L. Zhang, R. An, Z. Wang, L. Bao, and S. Chen, *J. Mater. Chem.*, **22**, 1489 (2012).
17. B. Qiu, J. Wang, Y. Xia, Z. Wei, S. Han, and Z. Liu, *ACS Appl. Mater. Interfaces*, **6**, 9185 (2014).
18. Y.-K. Sun, M.-J. Lee, C. S. Yoon, J. Hassoun, K. Amine, and B. Scrosati, *Adv. Mater.*, **24**, 1192 (2012).
19. J. Lee and W. Choi, *J. Electrochem. Soc.*, **162**, A743 (2015).
20. Y. Zhu, Y. Li, M. Bettge, and D. P. Abraham, *J. Electrochem. Soc.*, **159**, A2109 (2012).
21. J. A. Gilbert, J. Bareno, T. Spila, S. E. Trask, D. J. Miller, B. J. Polzin, A. N. Jansen, and D. P. Abraham, *J. Electrochem. Soc.*, **164**, A6054 (2017).
22. J. R. Croy, A. Gutierrez, M. He, B. T. Yonemoto, E. Lee, and M. M. Thackeray, *J. Power Sources*, **434**, 226706 (2019).
23. H. M. Cheng, F. M. Wang, J. P. Chu, R. Santhanam, J. Rick, and S. C. Lo, *J. Phys. Chem. C*, **116**, 7629 (2012).
24. J. Liu and A. Manthiram, *J. Electrochem. Soc.*, **156**, A833 (2009).

25. J. Liu and A. Manthiram, *J. Electrochem. Soc.*, **156**, A66 (2009).
26. Y. S. Jung, A. S. Cavanagh, Y. F. Yan, S. M. George, and A. Manthiram, *J. Electrochem. Soc.*, **158**, A1298 (2011).
27. Y. Zhu, Y. Li, M. Bettge, and D. P. Abraham, *Electrochim. Acta*, **110**, 191 (2013).
28. Y. Zhu, Y. Li, and D. P. Abraham, *J. Electrochem. Soc.*, **161**, A1580 (2014).
29. S. C. Wang, H. P. Hu, P. F. Yu, H. Y. Yang, X. H. Cai, and X. L. Wang, *J. Appl. Electrochem.*, **48**, 1221 (2018).
30. J. Wang, B. H. Toby, P. L. Lee, L. Ribaud, S. M. Antao, C. Kurtz, M. Ramanathan, R. B. Von Dreele, and M. A. Beno, *Rev. Sci. Instrum.*, **79**, 085105 (2008).
31. P. L. Lee, D. M. Shu, M. Ramanathan, C. Preissner, J. Wang, M. A. Beno, R. B. Von Dreele, L. Ribaud, C. Kurtz, S. M. Antao, X. Jiao, and B. H. Toby, *J. Synchrotron Radiat.*, **15**, 427 (2008).
32. L. R. Dalesio, J. O. Hill, M. Kraimer, S. Lewis, D. Murray, S. Hunt, W. Watson, M. Clausen, and J. Dalesio, *Nucl Instrum Meth A*, **352**, 179 (1994).
33. A. M. Andersson, D. P. Abraham, R. Haasch, S. MacLaren, J. Liu, and K. Amine, *J. Electrochem. Soc.*, **149**, A1358 (2002).
34. M. Winter and R. J. Brodd, *Chem. Rev.*, **105**, 1021 (2005).
35. S. Gantenbein, M. Weiss, and E. Ivers-Tiffee, *J. Power Sources*, **379**, 317 (2018).
36. A. Jossen, *J. Power Sources*, **154**, 530 (2006).
37. M. E. Orazem and B. Tribollet, *Electrochemical Impedance Spectroscopy*, Wiley, Hoboken, New Jersey (2017), p. 471.
38. R. Tatara, P. Karayaylali, Y. Yu, Y. R. Zhang, L. Giordano, F. Maglia, R. Jung, J. P. Schmidt, I. Lund, and Y. Shao-Horn, *J. Electrochem. Soc.*, **166**, A5090 (2018).
39. G. Assat, D. Foix, C. Delacourt, A. Iadecola, R. Dedryvere, and J. M. Tarascon, *Nat. Commun.*, 8 (2017).
40. R. Seeber, C. Zanardi, and G. J. C. Inzelt, **2**, 8 (2016).
41. B. A. Mei, J. Lau, T. Lin, S. H. Tolbert, B. S. Dunn, and L. Pilon, *J. Phys. Chem. C*, **122**, 24499 (2018).
42. Y. K. Lee, J. Park, and W. Lu, *J. Electrochem. Soc.*, **166**, A1340 (2019).
43. N. Schulz, R. Hausbrand, C. Wittich, L. Dimesso, and W. Jaegermann, *J. Electrochem. Soc.*, **165**, A833 (2018).
44. J. Im, J. Lee, M. H. Ryou, Y. M. Lee, and K. Y. Cho, *J. Electrochem. Soc.*, **164**, A6381 (2017).
45. N. Schulz, R. Hausbrand, L. Dimesso, and W. Jaegermann, *J. Electrochem. Soc.*, **165**, A819 (2018).
46. A. Gueguen, D. Streich, M. L. He, M. Mendez, F. F. Chesneau, P. Novak, and E. J. Berg, *J. Electrochem. Soc.*, **163**, A1095 (2016).
47. J. A. Gilbert, I. A. Shkrob, and D. P. Abraham, *J. Electrochem. Soc.*, **164**, A389 (2017).
48. B. R. Long, S. G. Rinaldo, K. G. Gallagher, D. W. Dees, S. E. Trask, B. J. Polzin, A. N. Jansen, D. P. Abraham, I. Bloom, J. Bareno, and J. R. Croy, *J. Electrochem. Soc.*, **163**, A2999 (2016).
49. J. Cha, J. G. Han, J. Hwang, J. Cho, and N. S. Choi, *J. Power Sources*, **357**, 97 (2017).
50. S. J. An, J. L. Li, C. Daniel, D. Mohanty, S. Nagpure, and D. L. Wood, *Carbon*, **105**, 52 (2016).

**Query**

Q1 AU: Please provide a digital object identifier (doi) for Ref(s) 9, 39, and 50. For additional information on doi's please select this link: http://www.doi.org/. If a doi is not available, no other information is needed from you